Palaeogeography, Palaeoclimatology, Palaeoecology 557 (2020) 109906

Contents lists available at ScienceDirect

Palaeogeography, Palaeoclimatology, Palaeoecology

journal homepage: www.elsevier.com/locate/palaeo

# Particle-size dependent magnetic properties of Scotia Sea sediments since the Last Glacial Maximum: Glacial ice-sheet discharge controlling magnetic proxies

Ji Young Shin[a,b], Sunghan Kim[b,*], Xiang Zhao[c], Kyu-Cheul Yoo[b], Yongjae Yu[d], Jae Il Lee[b], Min Kyung Lee[b], Ho Il Yoon[b]

[a] Deep-sea Mineral Resources Research Center, Korea Institute of Ocean Science and Technology, Busan 49111, Republic of Korea
[b] Korea Polar Research Institute, Incheon 21990, Republic of Korea
[c] Research School of Earth Sciences, Australian National University, Canberra, ACT 0200, Australia
[d] Department of Astronomy, Space Science, and Geology, Chungnam National University, Daejeon 34134, Republic of Korea

ARTICLE INFO

*Keywords:*
Magnetic property
Particle-size dependence
Southern Ocean
Glacial period
Iceberg-rafted debris

ABSTRACT

The strong glacial–interglacial similarity between the magnetic susceptibility (MS) of Southern Ocean sediments and Antarctic ice core dust records has often been used to reconstruct Southern Hemisphere atmospheric variability. Although evaluation of various magnetic properties is essential for identifying the magnetic carriers linked to sedimentological variation, detailed magnetic studies are not sufficient in the Scotia Sea. Here we investigate the bulk and particle-size dependent magnetic properties of Scotia Sea sediments over the past ~22 kyr, to determine the main sediment transport mechanism driving bulk magnetic proxies including MS. In bulk sediments, MS is highest during the last glacial period and is accompanied by an increase in the concentration and grain size of ferrimagnetic and antiferromagnetic minerals. For magnetic mineral assemblages, coarse detrital magnetite is dominant. Of three particle-size fractions (> 63, 16–63, and < 16 μm), the coarse silt fraction (16–63 μm) is responsible for the magnetic properties of bulk glacial sediments. Such dominant contribution of coarse silts rules out a major input of dust, which is expected as finer silt and clay. The silt fraction exhibits a co-varying magnetic mineral concentration with that of the sand fraction (> 63 μm) throughout the last deglaciation, indicating a close linkage between their input mechanisms. Thus, the sediment particles ranging from sand to coarse silt, which control the bulk glacial magnetic proxies, are most plausibly transported by iceberg-rafted debris (IRD). As hematite is relatively concentrated in the sand fraction, the hematite contribution in the bulk sediment can highlight IRD-related magnetic signals rather than magnetite. The bulk hematite contribution simultaneously varies with the deglacial influx of coarse IRD particles (> 1 mm) in Scotia Sea sediments, although their glacial inconsistency possibly suggests a different IRD input mechanism during the advancement and retreat of the ice sheet. Consequently, the glacial increase in the bulk magnetic concentration indicates vigorous iceberg calving activity in the Scotia Sea and further suggests the coupled cryosphere–atmosphere system.

## 1. Introduction

Terrigenous input to deep-sea sediment environments in the Southern Ocean relies on atmospheric and oceanic circulation patterns which are strongly influenced by climatic variability and Antarctic ice sheet dynamics. As a rapid and simple proxy of the terrigenous fraction, magnetic susceptibility (MS) of Southern Ocean sediments has revealed a close resemblance with Antarctic ice core dust records at the glacial–interglacial, or even, millennial scale (Bareille et al., 1994; Pugh et al., 2009; Weber et al., 2012). This strong resemblance plays a crucial role in relative age reconstruction of carbonate-poor Southern Ocean sediments (e.g., Weber et al., 2012). However, the MS–dust correlation, has not been fully understood in terms of transport mechanisms.

The Scotia Sea, located on the iceberg escape path from Antarctica and on the midway of dust transport from the known major source (Patagonia) to Antarctica (Delmonte et al., 2008), is very sensitive to paleoenvironmental change. MS of Scotia Sea sediments shows distinct glacial highs correlated to ice core dust records, and has been presumed

* Corresponding author.
*E-mail address:* delongksh@kopri.re.kr (S. Kim).

https://doi.org/10.1016/j.palaeo.2020.109906
Received 4 March 2020; Received in revised form 25 June 2020; Accepted 7 July 2020
Available online 18 July 2020
0031-0182/ 

as a proxy of Patagonian dust input (Weber et al., 2012). However, whether aeolian deposition is a major part of terrigenous fraction is a matter of debate, as it is expected to account for only a few percent of sediment accumulation during the last glacial period in the Scotia Sea (Walter et al., 2000; Noble et al., 2012). Apart from aeolian input, the Antarctic Circumpolar Current (ACC) has been suggested as the dominant sediment transporter delivering fine detritus during glacials, on a basis of clay mineralogy and isotopic composition (Diekmann et al., 2000, 2003; Noble et al., 2012; Xiao et al., 2016). On the other hand, Kim et al. (2018b) recently proposed iceberg-rafted debris (IRD) as the main deliver of glacial detrital particles, showing the dominance of coarse sediment fraction (fine sand to coarse silt) from particle-size analysis. These arguments still call for a better understanding of MS through systematic and detailed magnetic study in the Scotia Sea (Weber et al., 2019).

The MS signal is mainly carried by ferrimagnetic minerals, such as magnetite (Mullins, 1977; Maher, 1986), and basically connected to sediment magnetic properties (e.g., concentration, grain size, and composition of magnetic minerals). Since the magnetic properties of bulk sediments are an aggregate of many different components and processes, an evaluation of these components provides useful information on the bulk signals and sedimentary environments. For instance, Xiao et al. (2016) investigated bulk magnetic properties of Scotia Sea sediments and identified that detrital magnetite is the main magnetic component during glacials, whereas biogenic magnetite is significant during interglacials. With regard to low contribution of high-coercivity minerals, which commonly present in dust, they considered ocean-current transport of fine magnetic minerals as the main detrital input mechanism during glacials. However, detrital magnetic components complicatedly mixed by various processes (e.g., dust, current, and IRD) are not clearly discriminated in bulk magnetic properties in the Scotia Sea.

As an extended approach, magnetic measurements on particle-size fractions enable an isolation of magnetic property depending on particle-size distribution. As a result, the particle-size dependence of magnetic properties has been widely utilized to separate the influences of sediment transport and source in marine sediments (e.g., Razik et al., 2014, 2015; Hatfield et al., 2016, 2017, 2019). In this study, we adopt the particle-size separation approach to isolate detrital magnetic properties in Scotia Sea sediments since the last glacial maximum (LGM). By comparing bulk and particle-size dependent magnetic properties, we identify the major magnetic component and particle-size range carrying bulk signals, and determine the related sediment transport mechanism.

## 2. Core location and regional settings

An ~890 cm long gravity core GC03-C1 was recovered from the south Scotia Sea, off Elephant Island in the northern Antarctic Peninsula (60°26.57′S, 55°41.98′W; 3774- m water depth; Fig. 1) by R/V *Yuzhmorgeologiya* during the 2003/2004 Korea Antarctic Research Program expedition. The Scotia Sea is influenced by the input of waters from both the Drake Passage and the Weddell Sea, via the eastward-flowing ACC and northern limb of the Weddell Gyre, respectively (Fig. 1). Particularly, ACC is the dominant oceanic circulation in the Scotia Sea, responding to atmospheric changes, and it lies between the Polar Front and the southern ACC boundary (Anderson et al., 2009). In the Weddell Gyre, many icebergs merge and then escape from Antarctica north into the Scotia Sea along the major pathway named “Iceberg Alley” (Anderson and Andrews, 1999). In addition, the Southern Hemisphere westerlies dominate the atmospheric circulation of the Scotia Sea, delivering aeolian particles from southern Patagonia to proximal and far to distal regions in the Southern Ocean (Weber et al., 2012; Lamy et al., 2014). Thus, the Scotia Sea is sensitive to the terrigenous sediment supply via ocean currents, aeolian input, and ice rafting linked to climate change (Diekmann et al., 2000, 2003; Weber et al., 2014).

## 3. Analytical methods

### 3.1. Magnetic measurements and particle-size separation

The core was split into two halves at the Korea Polar Research Institute (KOPRI), and archive halves were used for magnetic measurements. Volume-specific MS (SI unit) data were previously reported by Bak et al. (2010), in which MS was scanned at 1 cm intervals for split half core sections. In this study, a total of 364 discrete samples for bulk sediment were taken with a nearly continuous ~2 cm span using 7 $cm^3$ plastic cubes. All cube samples were measured for mass-specific MS ($\chi$) at dual frequency of 470 Hz and 4700 Hz using a Bartington MS2 magnetometer at KOPRI. The mass normalization was calculated by wet masses; for wet samples, it should be noted that variance in $\chi$ can be somewhat different if dilution effect by the water mass is corrected. Hereafter $\chi$ in this paper refers to low frequency measurements ($\chi_{470Hz}$). Frequency dependence of MS ($\chi_{fd\%}$) was defined as $100 \times (\chi_{470Hz} - \chi_{4700Hz}) / \chi_{470Hz}$ (Dearing et al., 1996). Anhysteretic remanent magnetization (ARM) was imparted in a direct current (DC) field of 0.05 mT (= 39.79 A/m) and a peak alternating field (AF) of 100 mT using a D-Tech D-2000 AF demagnetizer (ASC Scientific). The mass-normalized ARM susceptibility ($\chi_{ARM}$) was calculated by normalizing the remanence to the DC field. The isothermal remanent magnetization (IRM) was acquired at applied DC fields of 1 T using an ASC Scientific IM-10 impulse magnetizer and is represented as saturation IRM (SIRM). Backfield IRM (BIRM) at 0.3 T was imparted in the direction opposite to that of SIRM. All remanences were measured using a JR6A spinner magnetometer at Chungnam National University, Korea.

$\chi$ and SIRM commonly reflect the concentration of ferrimagnetic minerals, such as magnetite. Because $\chi_{ARM}$ is sensitive to fine magnetite grains, $\chi_{ARM}/\chi$ was used as a grain size parameter (King et al., 1982). For the concentration of high-coercivity minerals such as hematite, hard IRM (HIRM) was calculated as follows: HIRM = 0.5 × (SIRM + BIRM). The relative composition of low- and high-coercivity minerals were estimated using S-ratios (Bloemendal et al., 1992): S-ratio = 0.5 × (1 – BIRM / SIRM). S-ratios close to 1 denote the dominance of low-coercivity minerals.

A total of 32 selected samples were freeze-dried, and hysteresis curves were measured using a Princeton Measurements MicroMag 3900 vibrating sample magnetometer at the Korea Institute of Geoscience and Mineral Resources. From the hysteresis data, the bulk coercive force ($B_c$), saturation magnetization ($M_s$), and saturation remanence ($M_{rs}$) were obtained by a saturating field of 1 T with field increments of 5 mT. Paramagnetic contribution was corrected using high-field slope at ≥80% of the peak field. The remanent coercive force ($B_{cr}$) values were determined from backfield measurements with a decreasing field step of 4 mT. For the magnetic mineralogy and assemblages, IRM acquisition curves and first-order reversal curves (FORCs) were measured for 18 selected samples. The IRM acquisition curves were obtained up to a DC field of 1.4 T with 120 nonlinear field steps and were fitted by modeled coercivity spectra using an IRM unmixing program from Maxbauer et al. (2016). 134 FORCs were obtained with a field increment of 2 mT up to a maximum applied field of 1 T and were processed in the FORCinel software package (Harrison and Feinberg, 2008) using the VARIFORC built-in function designed by Egli (2013).

In addition, 100 bulk sediment samples were collected from the top 400 cm at 4 cm intervals with a 1 cm span for particle-size separation. The sediments were pretreated with 6% hydrogen peroxide, 0.1 M hydrochloric acid, and 1 N sodium hydroxide to remove the non-terrigenous fractions (organic matter, carbonate, and biogenic opal, respectively). Some tested samples revealed no significant magnetization loss after such chemical treatments. This is consistent with previous studies that documented no physical or chemical alteration in magnetic mineral samples by weak to middle (e.g., pH ~ 4) acids (e.g., Hounslow and Maher, 1996; Maher et al., 2003; Strehlau et al., 2014). Based on

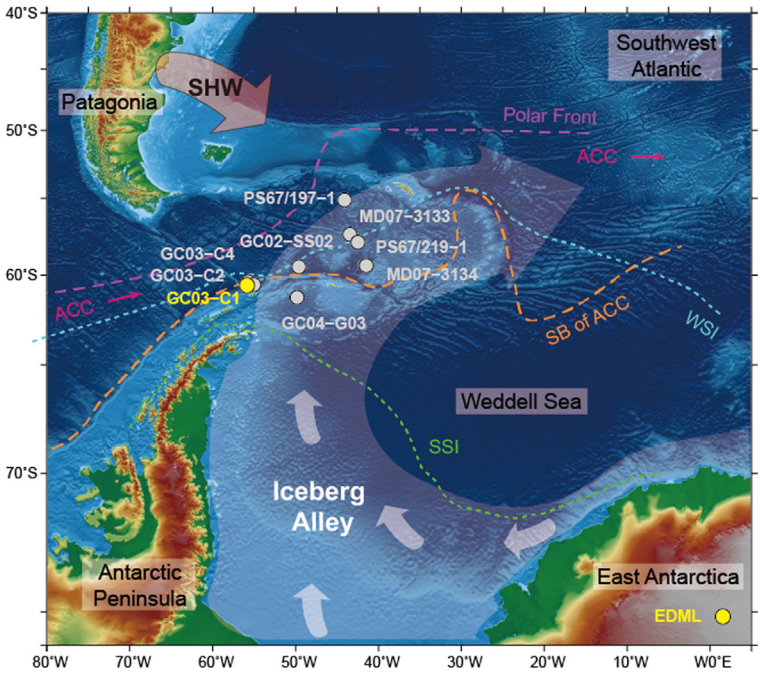


**Fig. 1.** Site location map for the studied core GC03-C1 (yellow dot) and reference sites (gray dots). Reference sites: GC03-C2, GC03-C4, GC04-G03, and GC02-SS02 from Kim et al. (2018b), MD07–3133 and MD07–3134 from Weber et al. (2012), and PS67/219–1 and PS67/197–1 from Xiao et al. (2016). Iceberg Alley from Anderson and Andrews (1999) is illustrated by white shaded arrows. The main wind direction of the Southern Hemisphere westerlies (SHW) is indicated by a red shaded arrow. Green and light blue dotted lines indicate the summer sea ice (SSI) and winter sea ice (WSI) sea-ice extent, respectively (Gersonde et al., 2005). The purple dotted line is the polar front, and orange dotted line is southern boundary of the Antarctic Circumpolar Current (SB of ACC; Orsi et al., 1995). ACC is shown by magenta arrows. (For interpretation of the references to colour in this figure legend, the reader is referred to the web version of this article.)

previous analyses for particle-size distribution in the study area (e.g., Kim et al., 2018b), three main fractions were separated by wet sieving at 63 μm and based on settling velocity: clay to fine silt (< 16 μm), medium to coarse silt (16–63 μm), and sand (> 63 μm). After weighing the dry mass of each fraction to calculate their fractional abundance (wt %), 300 samples (100 samples per fraction) were prepared for magnetic measurements. The sediment fractions were placed into gel capsules through compression to avoid grain rotation and then centered and fixated into 7 $cm^3$ cubes. The cube samples were subjected to χ measurements using a Kappabridge KLY-2 instrument at 920 Hz and field intensity of 300 A/m. Then, the same magnetic parameters with the bulk cube samples (e.g., ARM and IRM) were obtained. In addition, hysteresis curves and FORCs were measured for some selected samples.

### 3.2. Radiocarbon dating

Accelerator mass spectrometry (AMS) $^{14}C$ dates were measured at Rafter Radiocarbon Laboratory, New Zealand (Table 1). Because of the lack of foraminifers or calcareous shell fragments in the sediments, all AMS $^{14}C$ dating was conducted on acid insoluble organic matter (AIOM) from core GC03-C1. To correct for the core top loss, AIOM AMS $^{14}C$ dating was additionally conducted from 0 cm of a box core (BC03-C1) from the same location of GC03-C1 (Table 1).

## 4. Age model

An age model for core GC03-C1 was established by combination of the AIOM AMS $^{14}C$ dates and correlations among Scotia Sea MS records and the ice core dust record (Fig. 2). For $^{14}C$ age correction, the possible core top loss of GC03-C1 was estimated by comparing total carbon (TC), total nitrogen (TN), and water content (WC) between BC03-C1 and the top 100 cm of GC03-C1 (Fig. S1). Analytical procedures for TC, TN, and WC followed the common protocol in KOPRI (e.g., Kim et al., 2018a). Based on their inconsistent variations, a length of at least the box core, 32 cm, was thought to be lost during the coring process. As previous studies considered corrected $^{14}C$ dates after offsetting the surface AMS $^{14}C$ dates of AIOM, assuming that the old carbon effect was constant with depth (e.g., Domack et al., 1999; Lee et al., 2010), we corrected the AIOM ages of this study using the box core BC03-C1 top $^{14}C$ age of 4037 yr. This is older than the reservoir age (1300 years) used for the Scotia Sea (e.g., Xiao et al., 2016), indicating that the AIOM ages are influenced by old carbon effect. After offsetting 4037 yr, we obtained calibrated $^{14}C$ dates of GC03-C1 using CALIB 7.1 software (Stuiver and Reimer, 1993) and the MARINE13 dataset (Reimer et al., 2013) with a standard global reservoir age (ΔR = 0), following an approach of Lee et al. (2010) (Table 1). The relatively narrow $\delta^{13}C$ range ( ± 0.8‰ standard deviation) suggests that the assumption is generally acceptable. Of the calibrated $^{14}C$ ages, six age points within the deviation range were used to construct the age model for the top 200 cm of GC03-C1 (Table 1 and Fig. 2c, d). The $^{14}C$ ages below 240 cm were considered as less reliable and disregarded in the age model, because of old carbon effect in the glacial interval (e.g., Kim et al., 2018b).

In the Scotia Sea, the resemblance between MS records and dust record (non-sea-salt $Ca^{2+}$; $nssCa^{2+}$) from European Project for Ice Coring in Antarctica Dronning Maud Land (EDML) was used to constrain the age of the Scotia Sea sediment cores (Fischer et al., 2007; Weber et al., 2012). The MS–EDML correlation is particularly useful for the high MS intervals of Scotia Sea cores (e.g., Pugh et al., 2009; Weber et al., 2012; Xiao et al., 2016; Kim et al., 2018b). Following the age correlation established by Weber et al. (2012), we assigned seven tie points on volume MS of GC03-C1 (Bak et al., 2010), based on similar peaks and troughs in Scotia Sea MS records (cores MD07–3133 and MD07–3134; Fig. 1) and EDML dust record (Fig. 2 and Table 1). The core top and bottom ages of GC03-C1 were calculated as ~8.5 and ~22.1 ka, respectively, using extrapolation.

## 5. Results

### 5.1. Bulk magnetic properties

For the period ~22–8 ka, χ of GC03-C1 exhibits higher values during the LGM and lower values during the early Holocene (Fig. 3a). Water contents show a general opposite trend to χ, varying from ~50% at the upper part to ~30% at the lower part of the core (Table S1). Although correction for the water masses can increase χ values by a factor of ~2 to ~1.7, such dilution effect is not considered to be a critical factor because the trend of χ is analogous. $\chi_{fd\%}$ is generally below 2%, showing relatively low values during the LGM (Fig. 3b). This indicates that contribution of ultrafine superparamagnetic particles is not significant (Dearing et al., 1996), particularly for the glacial

**Table 1**
Acid insoluble organic matter radiocarbon dates from cores GC03-C1 and BC03-C1 and correlation points between GC03-C1 MS and EDML nss-$Ca^{2+}$ records.—*Ages used as tie points for the age model in this study. Corrected and calibrated ages are obtained using CALIB 7.1 software (Stuiver and Reimer, 1993) and the MARINE13 dataset (Reimer et al., 2013) with a standard global reservoir age (ΔR = 0) after subtracting the BC03-C1 top age of 4037 yr, following the approach in Lee et al. (2010). **Out-of-range ages.

| Depth (cm) | Lab code | $^{14}$C age (yr BP) | Error (yr) | $\delta^{13}$C (‰) | Corrected and calibrated age (2 σ) (cal. yr BP) | MS–EDML age (cal. yr BP) |
|---|---|---|---|---|---|---|
| *GC03-C1* | | | | | | |
| 10* | NZA-21383 | 12,290 | ± 45 | −24.9 | 8790 | |
| 30* | NZA-21384 | 12,788 | ± 45 | −25.8 | 9427 | |
| 50** | NZA-21466 | 16,169 | ± 65 | −25 | 13,581 | |
| 60* | NZA-21385 | 13,338 | ± 50 | −25.4 | 10,143 | |
| 100 | NZA-21467 | 13,209 | ± 50 | −25.6 | 9970 | |
| 120* | NZA-21386 | 13,749 | ± 50 | −26.4 | 10,613 | |
| 150* | NZA-21387 | 14,091 | ± 50 | −25.9 | 11,060 | |
| 181* | | | | | | 12,802 |
| 200* | NZA-21388 | 16,290 | ± 60 | −24.9 | 13,713 | |
| 240** | NZA-21468 | 18,519 | ± 80 | −26.9 | 17,118 | |
| 250* | | | | | | 14,797 |
| 311* | | | | | | 16,488 |
| 340* | | | | | | 17,628 |
| 350** | NZA-21469 | 21,900 | ± 110 | −27.4 | 21,085 | |
| 450** | NZA-21470 | 22,050 | ± 120 | −27.1 | 21,288 | |
| 478* | | | | | | 18,390 |
| 550** | NZA-21471 | 22,200 | ± 120 | −25.4 | 21,499 | |
| 650** | NZA-21472 | 23,470 | ± 130 | −25.3 | 22,908 | |
| 683* | | | | | | 20,046 |
| 750** | NZA-21549 | 21,430 | ± 120 | −24.9 | 20,487 | |
| 839* | | | | | | 21,617 |
| *BC03-C1* | | | | | | |
| 0 | NZA-21382 | 4037 | ± 30 | −25.9 | 0 | |

increase of χ.

Comparison between χ and other concentration-related magnetic parameters ($M_s$, SIRM, HIRM, and $\chi_{ARM}$) shows their consistent temporal variations (Fig. 3), supporting that concentration of magnetic minerals dominate changes in these parameters. Hysteresis loops were closed and $M_s$ was obtained in applied fields between ~350 mT during the LGM and ~270 mT during the early Holocene, indicating the dominance of ferrimagnetic minerals (e.g., magnetite, titanomagnetite, and maghemite). Hence, strong similarity among χ, $M_s$, and SIRM variations designates ferrimagnetic minerals as the dominant magnetic carrier of χ (Fig. 3a, c, d), although χ includes non-ferrimagnetic (i.e., diamagnetic and paramagnetic) signals. HIRM also varies with SIRM (Fig. 3d, e), indicating that both low- and high-coercivity minerals (e.g., magnetite and hematite, respectively) are closely related to the glacial increase in magnetic concentration. In particular, HIRM shows more distinct fluctuations than in SIRM during the marine isotope stage (MIS) 2, indicating relatively sensitive changes in high-coercivity mineral concentration during the glacial period. Meanwhile, $\chi_{ARM}$ resembles overall glacial–interglacial variations of the other parameters, showing large fluctuations during MIS 1 (Fig. 3f). This implies that fine magnetite concentration varies along with total magnetic concentration and more sensitively changes during the interglacial period. In addition, SIRM, HIRM, and $\chi_{ARM}$ display a common peak at 18.4 ka, which is inconspicuous in χ, indicating a layer of abundant ferrimagnetic minerals.

Generally, low values of the coercivity parameters $B_c$ and $B_{cr}$ (~8–12 and ~32–36 mT, respectively) suggest that magnetite is the main magnetic carrier (Fig. 4a, d). In particular, low $B_c$ values of ~9 mT during the LGM indicate the dominance of low-coercivity coarse magnetite, such as multidomain (MD) magnetite (Maher, 1988). Other magnetic grain size parameters ($M_{rs}/M_s$ and $\chi_{ARM}/\chi$) also show similar variations with $B_c$, indicating that coarser magnetite is dominated during the LGM (Fig. 4b, c). On the other hand, $B_{cr}$ shows analogous variations with S-ratio (Fig. 4d, e), as $B_{cr}$ is more sensitive to high-coercivity components than $B_c$ in magnetic mixtures (Roberts et al., 1995). The S-ratios close to 1 (~0.97–0.99) throughout the core indicate the generally low contribution of high-coercivity minerals (e.g., hematite). However, relatively low S-ratios during MIS 2 indicate their greater contribution during the glacial period. There are some $B_{cr}$ peaks to ~40 mT concurrent with the S-ratio troughs during MIS 2 (e.g., ~15.9 ka, ~18.4 ka, and ~20.5 ka), supporting the presence of high-coercivity minerals (Fig. 4d, e).

The average magnetite grain size distribution (i.e., hysteresis ratios) for the selected samples is compared with empirical and theoretical data in a Day plot (Day et al., 1977; Fig. 5a). All the samples fall close to the theoretical mixing curves of single-domain (SD) and MD, with relative dominance of MD (Carter-Stiglitz et al., 2001; Dunlop and Carter-Stiglitz, 2006). Compared with empirical data of (unannealed) magnetite (Dunlop, 2002), the average grain size of our samples corresponds to a range from ~9 to > 20 μm, with grain size coarsening for the glacial samples. To further identify magnetic mineral assemblages, FORC diagrams were constructed (Fig. 5b). Along with the coarse average grain size, the interglacial sample (~10.2 ka) shows a large triangular vertical spread at low coercivity, indicating the dominance of vortex state detrital magnetite (Roberts et al., 2014, 2017). A typical narrow central ridge along the $B_c$ axis characterizes the presence of non-interacting bacterial SD magnetite (Egli et al., 2010). Meanwhile, the glacial sample (~19.6 ka) is characterized by a stronger vertical spread at low coercivity ($B_c$ < 20 mT), which confirms the greater contribution of coarser vortex/MD magnetite during the LGM. For the glacial sample, a high-coercivity component extends beyond 100 mT along the $B_u$ axis. From the IRM unmixing results, the high-coercivity component has a mean coercivity of 201–212 mT (cp3, Fig. 5c), consistent with the coercivity range of hematite (Hyland et al., 2015). The hematite contribution is relatively low (~6–12% of SIRM) but is greater in the glacial sample. In addition, two low-coercivity components (cp1 and cp2) are considered as magnetites of different coercivities (Egli, 2003).

In summary, the magnetic mineral concentration of GC03-C1 is high during the glacial period and low during the interglacial period. The dominant magnetic component is magnetite, showing coarser magnetic grain size during the glacial period. For magnetic mineral assemblages, coarse vortex/MD state detrital magnetite is dominant during the glacial period. During the interglacial period, the contribution of non-

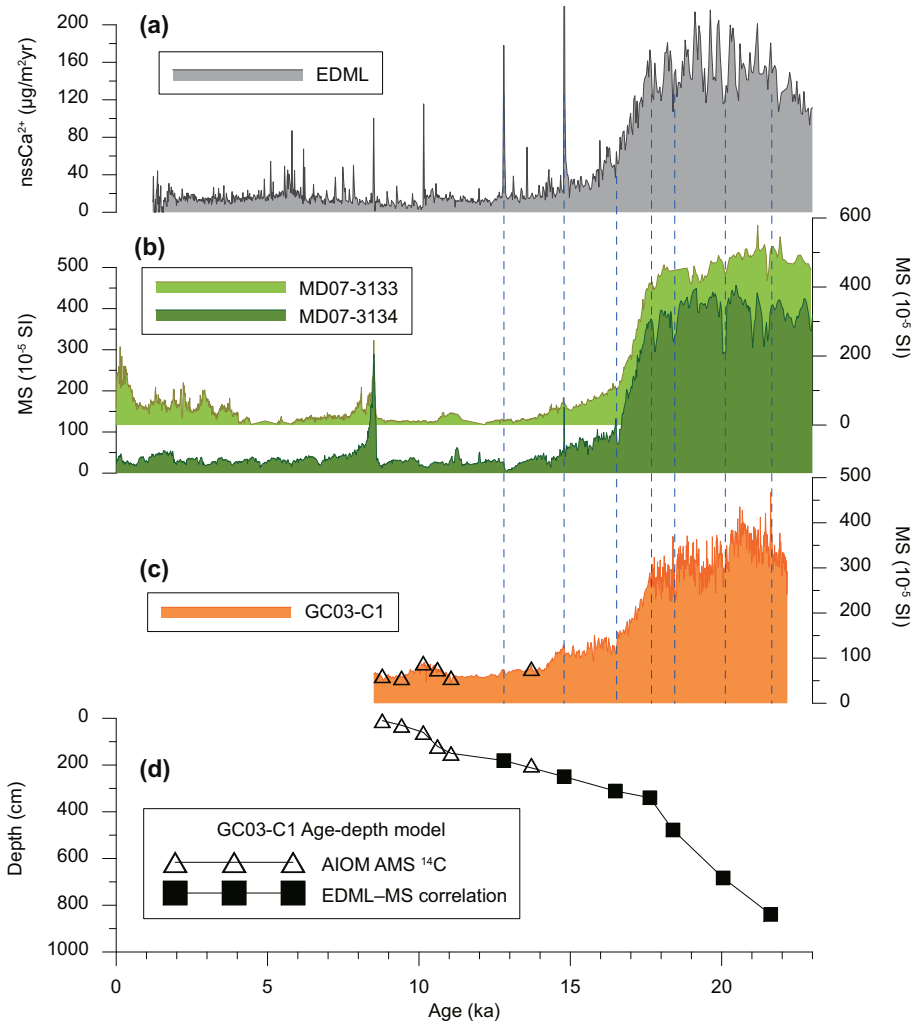


**Fig. 2.** Age control for core GC03-C1. (a) EDML ice core non-sea-salt $Ca^{2+}$ ($nssCa^{2+}$) flux, dust record (Fischer et al., 2007); (b) magnetic susceptibility (MS) of cores MD07–3133 and MD07–3134 (Weber et al., 2012); (c) MS of GC03-C1 (Bak et al., 2010); and (d) final age–depth model of GC03-C1 based on the EDML–MS correlations combined with $^{14}C$ dates for the top 200 cm. The $^{14}C$ dates are marked as open triangles and the correlation tie points are shown as closed squares.

interacting biogenic SD magnetite is relatively significant, along with the dominance of vortex detrital magnetite. The hematite contribution is generally low, but relatively high during the glacial period.

### 5.2. Magnetic concentration of particle-size fractions

For the last ~18 kyr, concentration-related magnetic parameters ($\chi$, $M_s$, SIRM, $\chi_{ARM}$, and HIRM) for each sized fraction were obtained and compared with their respective bulk values (Fig. 6). The magnetic parameters were calculated as mass-normalized values (Figs. 6b–f), and then mass-weighted (Figs. 6g–k) by multiplying each fractional mass percent (Fig. 6a) on the mass-normalized values. The mass-normalized values indicate magnetic mineral enrichment in the fractions, while the mass-weighted values reconstruct the fractional contribution to the bulk values, as magnetic concentration properties are linearly additive (e.g., Lascu et al., 2010; Hatfield et al., 2019). The fractional mass distribution shows that the 16–63 μm fraction is predominant (50–70%) (Fig. 6a). Noticeably, the 16–63 μm and > 63 μm relative abundances becomes greater during MIS 2 than during MIS 1, confirming the coarsening of average particle size during the glacial period.

The most abundant fraction, 16–63 μm, generally shows the highest mass-normalized $\chi$ values throughout the last ~18 ka (Fig. 6a, b) and, thus, makes the greatest contribution to bulk $\chi$. This is confirmed by the almost identical variations between mass-weighted $\chi$ of the 16–63 μm fraction and bulk $\chi$ (Fig. 6g). $M_s$ values (after paramagnetic correction) for the three fractions show similar variations with $\chi$ (Fig. 6b, c), confirming that the $\chi$ variation is mainly controlled by the magnetite concentration. The highest $M_s$ of the 16–63 μm fraction during the glacial period indicates that magnetite is the most-enriched in silts (Fig. 6h), regardless of magnetic grain size (Day et al., 1977; Dunlop, 1986).

Mass-normalized SIRM of each fraction also shows similar temporal variations with $\chi$ (Fig. 6b, d); however, the SIRM signals are not the highest for the 16–63 μm fraction. As SIRM is affected by magnetic grain size, coarse magnetites in 16–63 μm can be less respondent to SIRM than $\chi$, owing to their weak magnetic remanence (Maher, 1988). Nevertheless, the strongest SIRM values in the > 63 μm fraction during MIS 2 indicates glacial magnetic mineral enrichment with strong magnetic remanence. In particular, SIRM of the three particle-size fractions is comparable throughout the last deglaciation (Fig. 6d), clearly indicating that most of the magnetic minerals are closely linked to the same input mechanism. Owing to its fractional abundance, the 16–63 μm fraction dominantly contributes to bulk SIRM (Fig. 6i).

As $\chi_{ARM}$ is mainly carried by fine magnetite, the finest grain size fraction (< 16 μm) has the highest values (Fig. 6e). The < 16 μm fraction consistently shows the highest $\chi_{ARM}$ with severe fluctuation throughout the last ~18 kyr, while the two coarser fractions show similar $\chi_{ARM}$ variations with SIRM (Fig. 6e). The different temporal

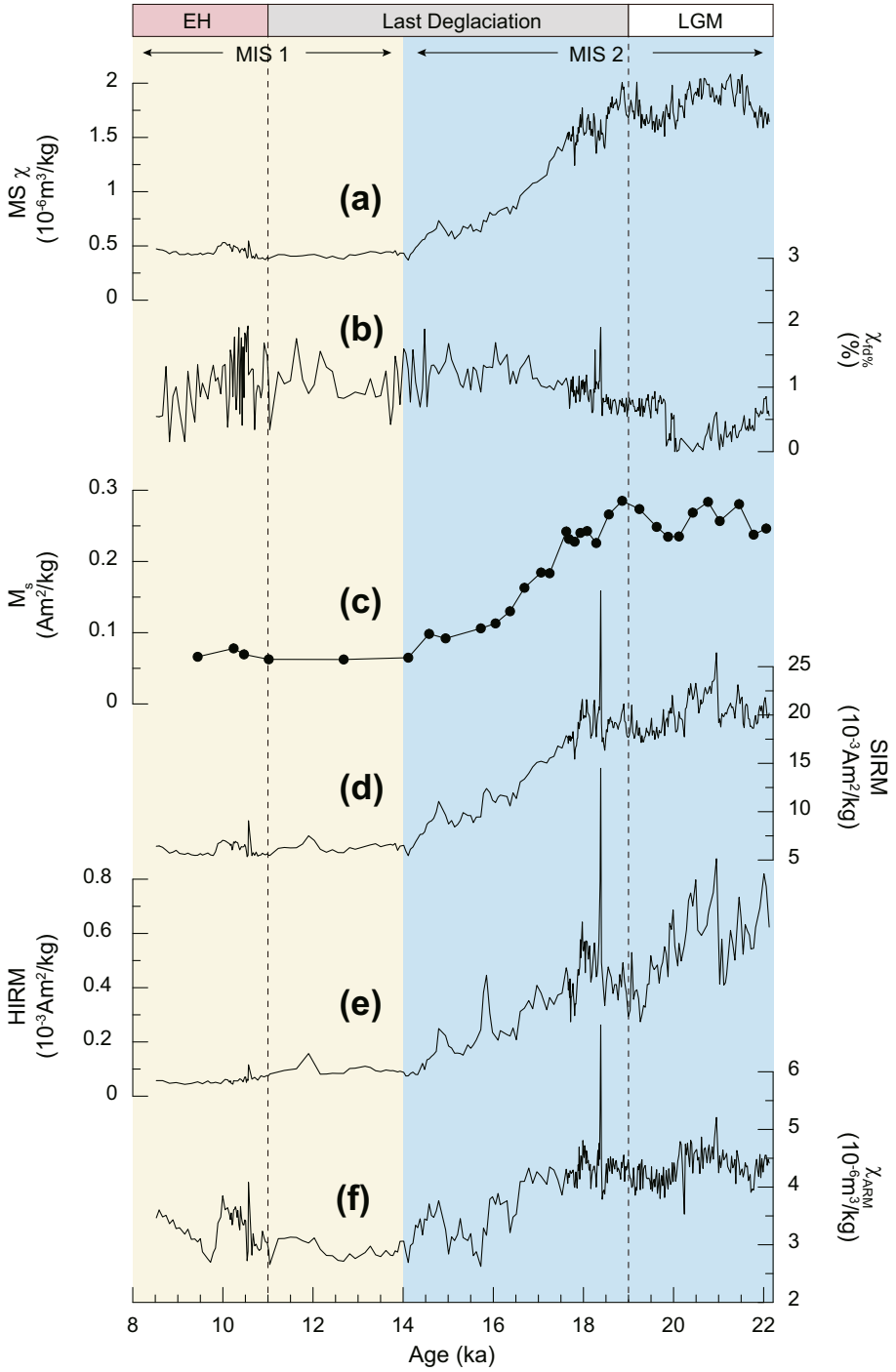


**Fig. 3.** Temporal variations of magnetic concentration parameters for GC03-C1. (a) Mass-specific MS ($\chi$); (b) frequency-dependent $\chi$ ($\chi_{fd\%}$); (c) saturation magnetization ($M_s$); (d) saturation isothermal remanent magnetization (SIRM); (e) hard IRM (HIRM); and (f) susceptibility of anhysteretic remanent magnetization ($\chi_{ARM}$). Yellow and blue bars indicate MIS 1 and 2, respectively. Three paleoclimatic events (the Early Holocene (EH), the Last Deglaciation, and the LGM) are labeled at the top. (For interpretation of the references to colour in this figure legend, the reader is referred to the web version of this article.)

variations of the < 16 μm fraction can be affected by different magnetic sources (e.g., biogenic magnetite) compared to the coarser fractions, particularly during MIS 1. Although bulk $\chi_{ARM}$ is mainly contributed by the < 16 μm fraction, the glacial increase of bulk $\chi_{ARM}$ is associated with an increase in the contribution of the 16–63 μm fraction (Fig. 6j).

The highest HIRM values in the > 63 μm fraction reveal that hematite is the most concentrated in the coarse sand fraction (Fig. 6f). The 16–63 μm fraction has markedly low HIRM (Fig. 6f) but dominantly contributes to bulk HIRM (Fig. 6k), owing to its high fractional abundance. The HIRM variations between 16 and 63 μm and > 63 μm are very similar during MIS 2 (Fig. 6f, k), indicating the same input source of hematite. Moreover, such HIRM variations are analogous to those of all other parameters (Figs. 6b–k), suggesting that the concentration of magnetite and hematite is mostly linked to the same input of sediment, ranging from sand to coarse silt.

### 5.3. Magnetic mineralogy and grain size of particle-size fractions

The bulk and size-fractionated samples were selected at ~17.7 ka and constructed FORC diagrams to confirm their magnetic assemblages

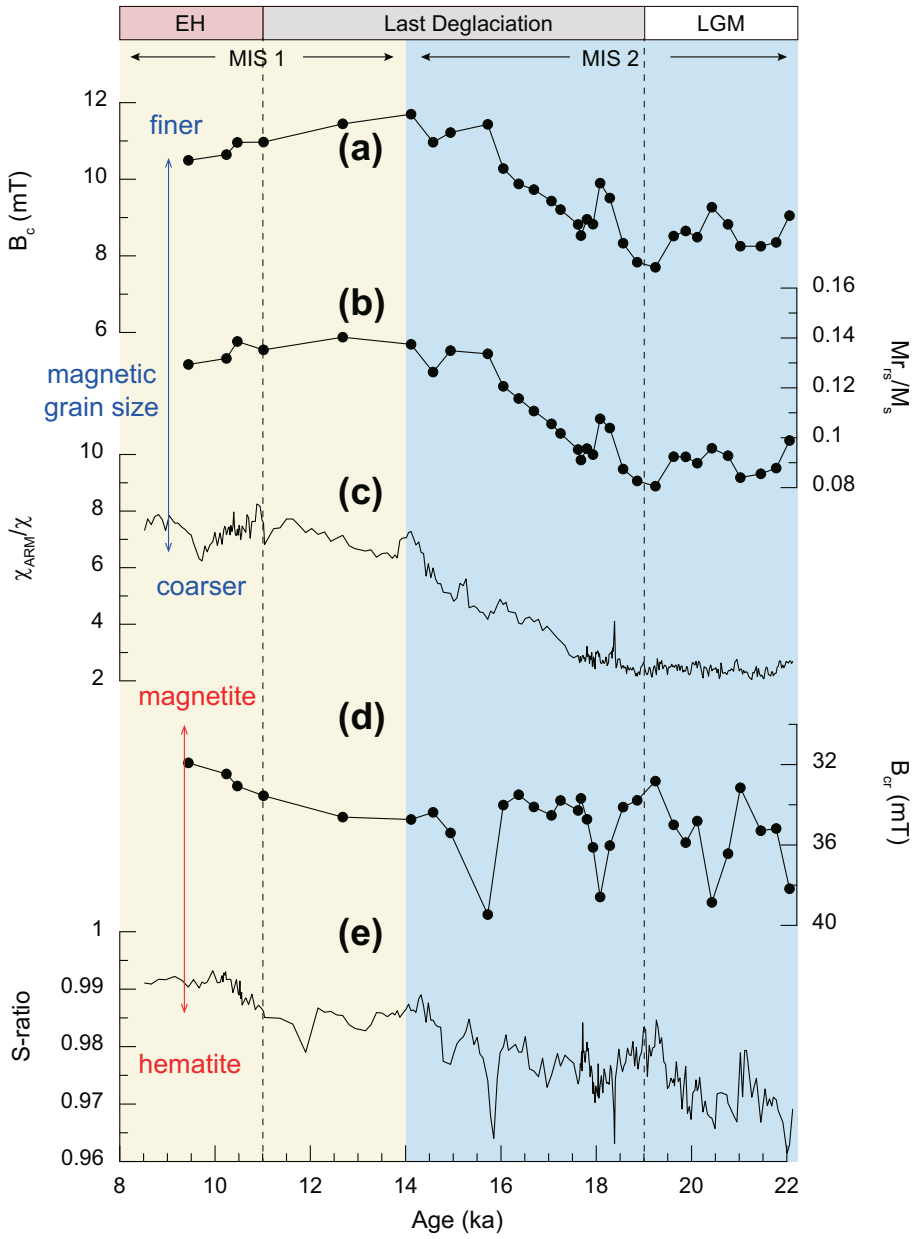


**Fig. 4.** Temporal variations of magnetic composition and grain size parameters. (a) Coercive force ($B_c$), (b) saturation remanence ($M_{rs}$) relative to $M_s$, and (c) $\chi_{ARM}/\chi$ indicate magnetic grain size variations. (d) Remanent coercivity ($B_{cr}$) and (e) S-ratio reflect the relative compositions of magnetite and hematite.

(solid symbols in Fig. 7a). FORC diagrams of the bulk and 16–63 μm fraction resemble each other, showing the dominant feature of coarse vortex/MD magnetite (i.e., triangular-shaped contour with large vertical spread). The < 16 and > 63 μm fractions are dominated by finer vortex state magnetite. For the < 16 μm fraction, the central ridge signal remains. This indicates a good preservation of biogenic magnetite during the glacial period, although its contribution is largely diluted in the bulk glacial samples (Figs. 7a and 5b). For > 63 μm, the SD-like isolated peak with vortex magnetic feature ensures the presence of fine magnetic inclusions (Roberts et al., 2014, 2017). In addition, a large contribution of hematite with higher coercivity (> 100 mT) is distinctively observed in this fraction (Fig. 7a).

For each fraction, 11 samples were selected for hysteresis analyses, and their magnetic grain sizes were viewed on a Day plot (Fig. 7b). Note, the magnetic grain size is based on magnetic properties (i.e., domain state), which should not be confused with physical particle size (Hatfield et al., 2017). Hysteresis ratios of the < 16 μm (blue symbols in Fig. 7b) and 16–63 μm (red symbols in Fig. 7b) fractions are well clustered and comparable to ratios of 3–6 μm and > 14 μm magnetite grains, respectively (Dunlop, 2002). The < 16 and 16–63 μm fractions also fall on the theoretical SD-MD mixing line (Carter-Stiglitz et al., 2001; Dunlop and Carter-Stiglitz, 2006), with greater MD contribution in the 16–63 μm fraction. Meanwhile, the > 63 μm fraction displays a wide distribution of hysteresis ratios that fall between those of the < 16 and 16–63 μm fractions (yellow symbols in Fig. 7b). The ratios are also dominantly distributed close to those of the < 16 μm fraction, corresponding to 6–9 μm magnetite grains (Dunlop, 2002). This decoupling of physical and magnetic grain sizes indicates that magnetic minerals in the sand fraction are dominantly present as inclusions in other minerals, such as silicates (e.g., Feinberg et al., 2005; Chang et al., 2016), rather than as discrete magnetite grains.

Compared with bulk hysteresis ratios at the same ages (magenta symbols in Fig. 7b), the ratios of the 16–63 μm fraction show a large overlap with those of coarser glacial bulk samples. This indicates that

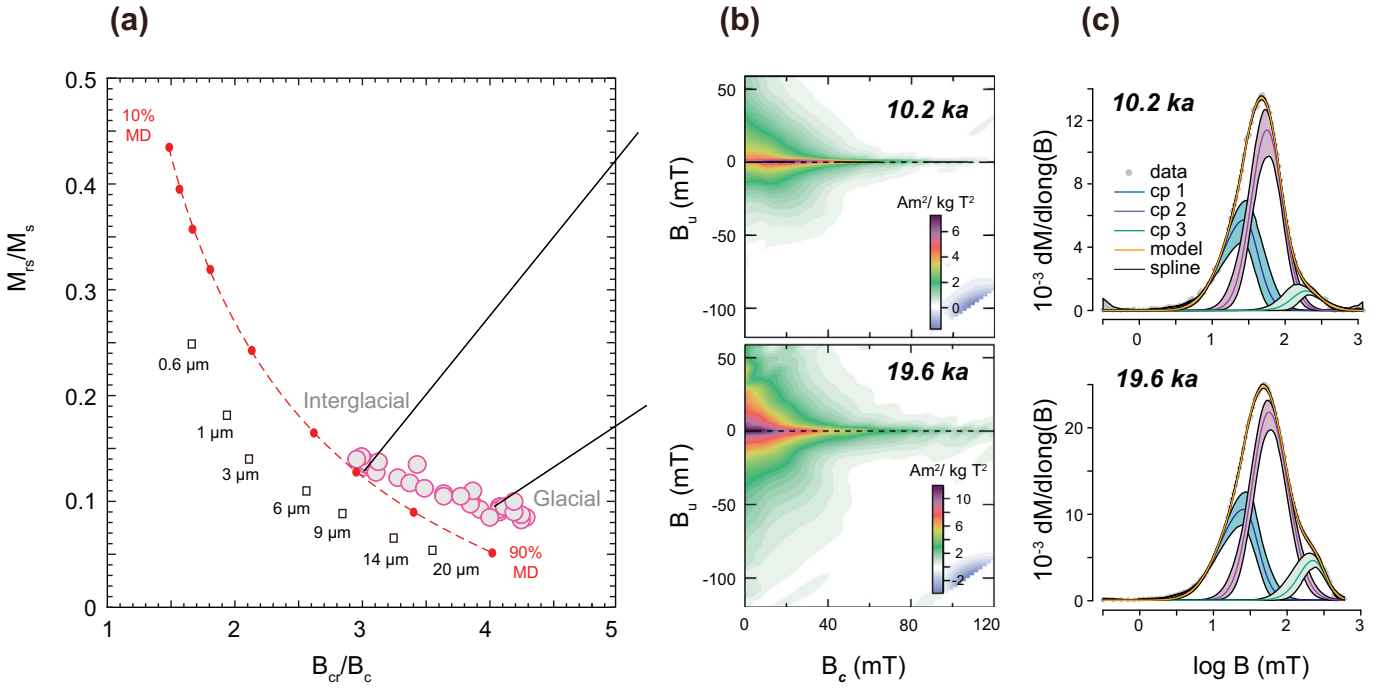


**Fig. 5.** Magnetic grain size and magnetic mineral assemblages for selected bulk sediment samples. Hysteresis ratios (magenta circles) are plotted in the (a) Day plot (Day et al., 1977). The sample ages for hysteresis ratios are the same in Fig. 4b. Red dotted line is a theoretical mixing line of single-domain (SD) and multidomain (MD) magnetite (Carter-Stiglitz et al., 2001; Dunlop and Carter-Stiglitz, 2006). Open squares are hysteresis ratios from unannealed natural-sized titanomagnetite (Dunlop, 2002). For representative interglacial (10.2 ka) and glacial (19.6 ka) samples, (b) FORC diagrams are plotted as $B_c$ versus interaction field ($B_u$), and (c) IRM coercivity spectra were modeled using three components (cp 1 in blue, cp 2 in purple, and cp 3 in green in order of magnitude). Gray symbols are our data, and the black line is the spline fit. Shaded envelopes represent 95% confidence intervals. (For interpretation of the references to colour in this figure legend, the reader is referred to the web version of this article.)

the silt fraction is the predominant magnetic carrier during the glacial period, which is also supported by the resemblance of FORC diagrams between the bulk sample and the 16–63 μm fraction (Fig. 7a). Hence, the coarsening of bulk magnetic grain size in the glacial period is resulted from the increased contribution of coarse vortex/MD magnetic minerals in silts.

## 6. Discussion

### 6.1. Comparison of Scotia Sea rock-magnetic properties with dust records

Long-range dust transport from Patagonia to East Antarctica during the Pleistocene is traced by a dust proxy ($nssCa^{2+}$) from the EDML ice cores (e.g., Fischer et al., 2007, Fig. 8a). The glacial increase in Antarctic dust concentration indicates enhanced Patagonian dust production related to various factors, such as exposure of the source area and evolution of the southern westerly wind belt (Lamy et al., 2010; Lambert et al., 2012). As previously reported in the Scotia Sea, MS variations of core GC03-C1 and Scotia Sea cores (Weber et al., 2012; Xiao et al., 2016) are very similar to EDML $nssCa^{2+}$ (Figs. 8a–d); volume MS records were used for comparison among cores. This visual resemblance between MS and Antarctic dust records seems to reflect the sink of Patagonian dust into the Scotia Sea and Antarctica (e.g., Weber et al., 2012). However, the particle-size range of 16–63 μm, suggested as the main contributor to the MS signal of GC03-C1, is coarser than fine aerosol particles of < 10 μm which are generally expected to be long-range transported (Maher et al., 2010; Muhs, 2013).

As a proximal record of Patagonian dust from the source, MS of a sediment core from the PASADO site 2 at Laguna Potrok Aike in Patagonia (Lisé-Pronovost et al., 2015) is also compared. The lacustrine sediments reflect the deposition of short-term suspended dust particles of tens to hundreds of kilometers in the distance. Lisé-Pronovost et al. (2015) presented that the Patagonian lake sediments show glacial–interglacial MS variations covariant with the dust record of the Antarctic ice core (Fig. 8a, e), although there is an inconsistency in the millennial scale. They suggested that the glacial increase in the two records reflects a common response to the aeolian flux from the source area; the higher magnetic concentration is associated with the greater aeolian supply. The millennial inconsistency was suggested as grain size effect on MS, because the glacial high MS of the lake sediments is also correlated to higher coercivity of ferrimagnetic grains (i.e., increase in median destructive field of IRM; Fig. 8e), reflecting a fining of magnetic grain size due to weakening of the Southern Hemisphere westerly winds (Kohfeld et al., 2013; Lisé-Pronovost et al., 2015). For long-range transported dust to the Scotia Sea and Antarctica, the particle-size is independent of the change in wind intensity (Muhs, 2013), but it should be generally smaller than the Patagonian lake sediments. Lisé-Pronovost et al. (2015) identified that medium and coarse silts (~10–30 μm) mainly carry the magnetic information of the lake sediments, suggesting that dust transport to the Scotia Sea would involve finer particles, such as fine silt and clay. This implies that glacial sediments of GC03-C1 are unlikely transported primarily by Patagonian dust, as the high magnetic concentration is mostly carried by medium to coarse silts (16–63 μm).

In the south Scotia Sea, the particle-size distribution with the dominance of medium to coarse silt in glacial sediment was consistently reported from four nearby cores (GC03-C2, GC03-C4, GC04-G03, and GC02-SS02; Fig. 1), based on particle-size analysis (Kim et al., 2018b). For magnetic grain size, LGM sediments of GC03-C1 dominated by coarse vortex/MD magnetite have similar hysteresis ratio distribution with the central Scotia Sea sediments (PS67/219–1 and PS67/197–1; Fig. 1) during glacials (Xiao et al., 2016; Fig. S2). This coarse magnetic grain size distribution of the glacial Scotia Sea sediments is also comparable with that of the Laguna Potrok Aike sediments (Lisé-Pronovost

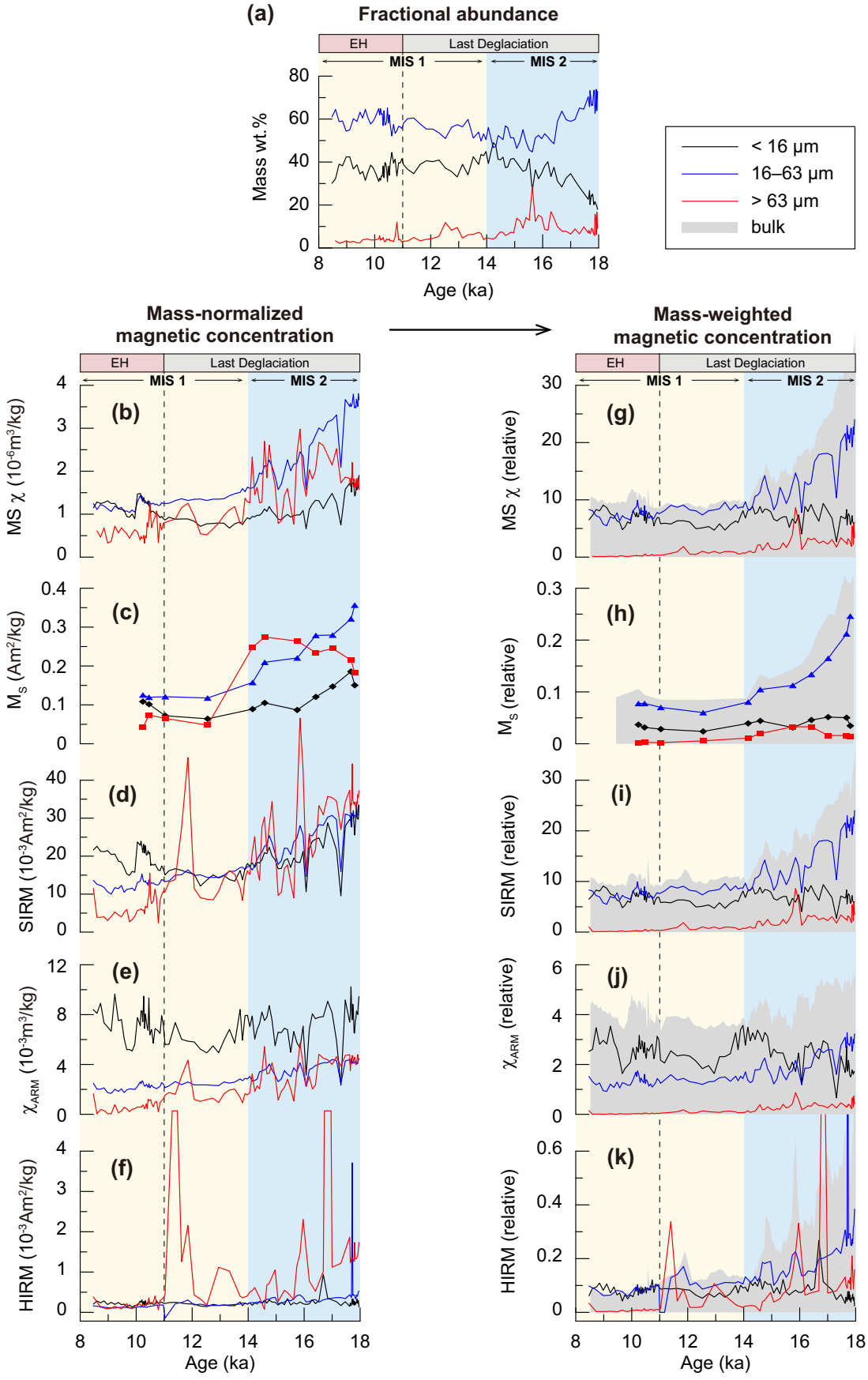


**Fig. 6.** Fractional abundance and magnetic concentration parameters ($\chi$, $M_s$, SIRM, $\chi_{ARM}$, and HIRM) of sediment particle-size fractions for the last ~18 kyr. (a) Dry-mass weight percent (wt%) for three sized fractions (< 16 μm in black, 16–63 μm in blue, and > 63 μm in red) indicates the fractional abundance. For each fraction, variations of (b–f) mass-normalized and (g–k) mass-weighted magnetic concentration parameters are presented. The same parameters for bulk sediment are shown as gray shaded in the right panel for comparison. (For interpretation of the references to colour in this figure legend, the reader is referred to the web version of this

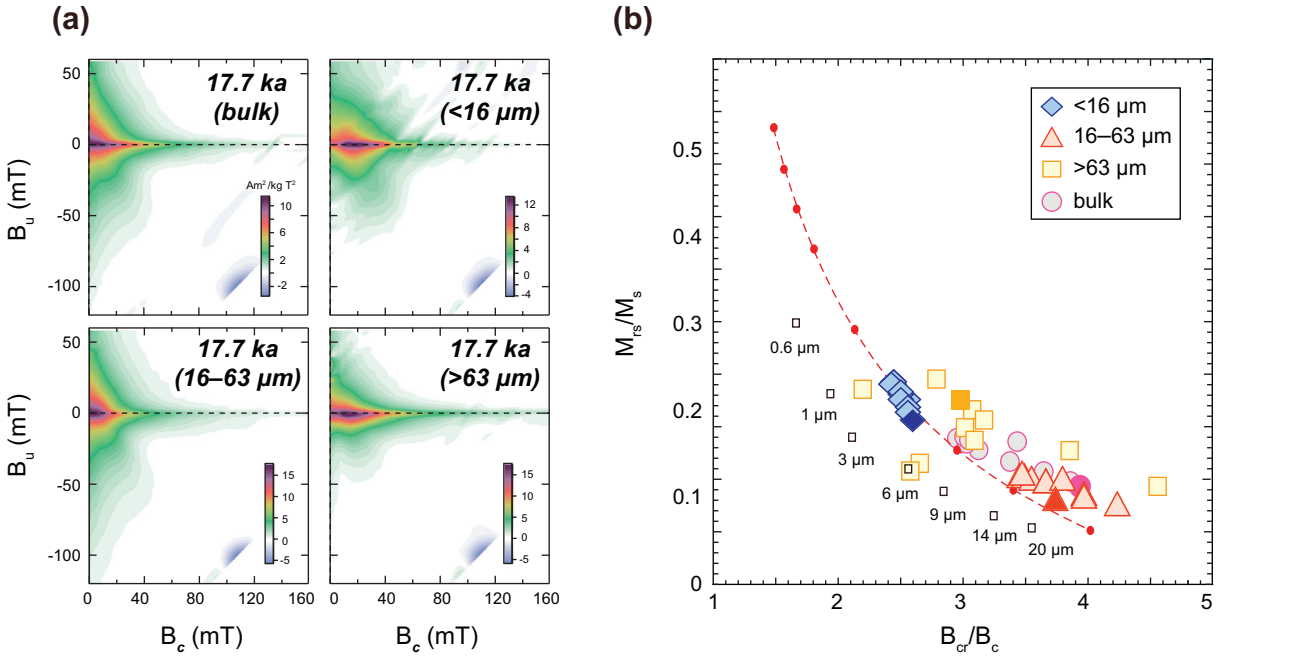


**Fig. 7.** Magnetic mineral assemblages and grain sizes for selected bulk sediment samples and their particle-size fractions. (a) FORC diagrams for bulk and size-fractionated samples at ~17.7 ka are presented. (b) In the Day plot, hysteresis ratios of three fractions (< 16 μm, 16–63 μm, and > 63 μm) are marked in blue diamonds, red triangles, and yellow squares, respectively. The sediment ages of 11 samples for each fraction correspond to ~10–18 ka, as the same in Fig. 6c. The bulk hysteresis ratios at the same ages are shown as magenta circles for comparison, and closed symbols corresponds to 17.7 ka samples for the FORC diagrams. See caption of Fig. 5 for the description of the Day plot and FORC diagrams. (For interpretation of the references to colour in this figure legend, the reader is referred to the web version of this article.)

et al., 2015), which were deposited by short-term transport during the last glacial period (Fig. S2). Altogether, these results show general agreement in the coarse physical and magnetic grain size of the glacial sediments in the Scotia Sea and rule out dust input as the main sediment transport mechanism during the glacial period.

Interestingly, the < 16 μm fraction of GC03-C1 has a very low hematite concentration (Figs. 6f and 7a), although it is expected to primarily contain the aeolian dust fraction. Rather, the hematite contribution in the glacial bulk sediments is associated with the coarser sand and silt fractions (Fig. 6k). Therefore, the bulk hematite concentration should not be considered as an indication of dust input, because of its low contribution in the Scotia Sea, although aeolian dust generally involves high-coercivity minerals such as hematite (e.g., Bloemendal et al., 1992; Xiao et al., 2016).

### 6.2. Contribution of biogenic magnetite in Scotia Sea sediments

Biogenic magnetite has been suggested as a dominant contributor to the MS signal in the sub-Antarctic Indian Ocean, where low detrital input occurs; it could be associated with iron fertilization caused by increased dust input during glacials (Yamazaki and Ikehara, 2012). However, the relative proportion of biogenic magnetite to detrital magnetite in bulk sediments of GC03-C1 decreases during the glacial period (Fig. 5b), as consistently shown in the central Scotia Sea sediments (Xiao et al., 2016). Although biogenic magnetite is not the main magnetic carrier during the glacial period, the glacial < 16 μm sample displays a significant contribution of biogenic magnetite compared to the bulk sample largely diluted by coarse detrital magnetite (Fig. 7a). The glacial increase in biogenic magnetite is not noticeable, but the presence of biogenic magnetite implies a suitable environment for its production and/or preservation during the glacial period.

### 6.3. Implications for possible sediment transport environments

The particle-size dependent magnetic properties of core GC03-C1 indicate that coarse sediments (sands and silts) are mainly transported by the same mechanism during the glacial period, with strong magnetic remanence in sands (Fig. 6d, f). The glacial dominance of sediment particles ranging from fine sand to medium silt is consistently reported from the nearby cores in the south Scotia Sea (Kim et al., 2018b). These results indicate that the main terrigenous supply mechanism during the glacial period dominantly delivers coarse detrital particles in the range of sand to silt to the Scotia Sea.

Several studies have suggested that ocean currents play an important role in sediment transport during glacials in the Scotia Sea (e.g., Diekmann et al., 2000, 2003; Noble et al., 2012; Xiao et al., 2016). In the Scotia Sea, ACC carries suspended terrigenous materials from the Antarctic Peninsula and Patagonia and disperses continental detritus through the Drake Passage (Diekmann et al., 2000; Hemming et al., 2007). During glacials, enhanced current erosion in extended terrigenous source areas at low sea level stands could provide more detrital materials to the sea (Noble et al., 2012; Xiao et al., 2016). However, sediment supply by current erosion is generally expected to deliver fine-grained detritus (e.g., silt and clay) to deep-sea environments (e.g., Diekmann et al., 2000; Noble et al., 2012), as the lateral transport of > 63 μm particles requires turbulence of higher velocities than is often available in the deep sea. Therefore, current transport of the dominant sand- to medium-silt-sized fractions in the glacial sediments should be accompanied by enhanced ACC intensity; however, ACC intensity was reportedly weaker during the glacial period than during the Holocene in the Scotia Sea and the Drake Passage (McCave et al., 2014; Lamy et al., 2015; Jouve et al., 2017). For instance, the fine sand fraction in sediments from the southernmost continental margin of South America significantly decreased during the glacial period, reflecting weak ACC intensity (Lamy et al., 2015). This implies that the glacial ACC was not strong enough to deliver sands from South America

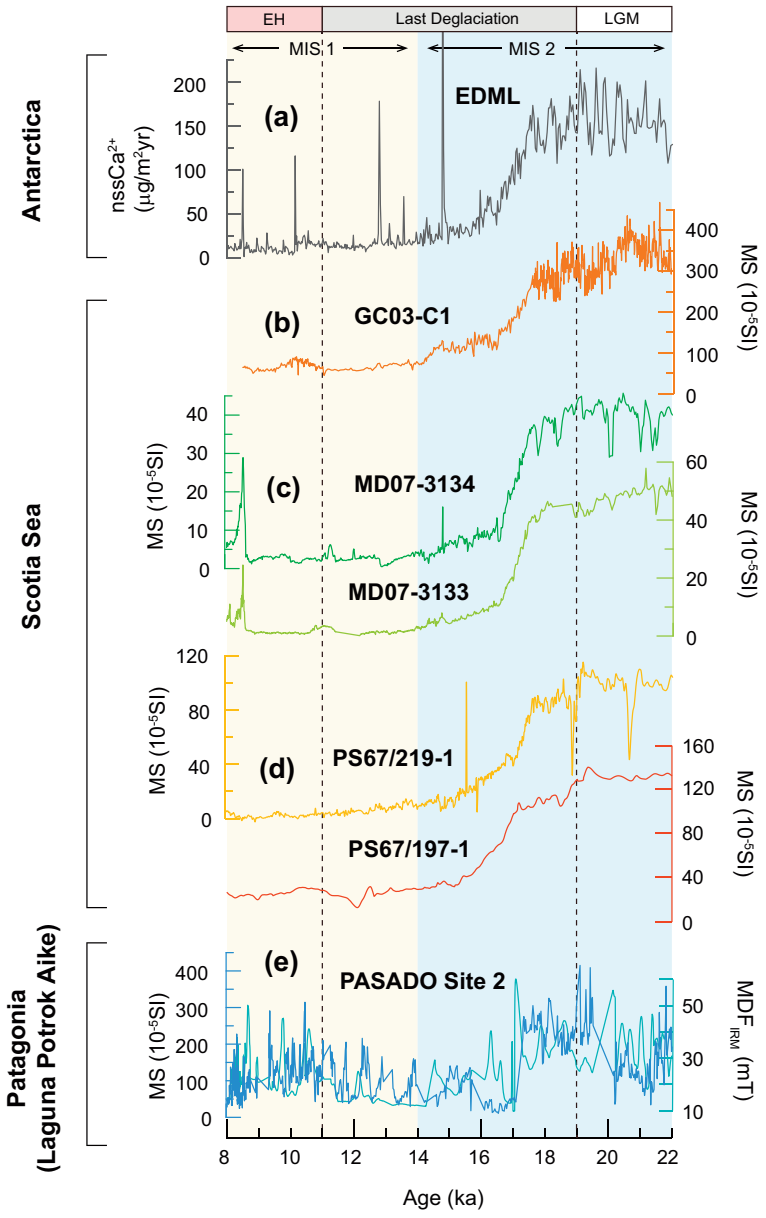


**Fig. 8.** Comparison among Antarctic ice core dust record and MS records in the Scotia Sea and Patagonia. (a) Non-sea-salt $Ca^{2+}$ ($nssCa^{2+}$) flux of EDML ice core from Antarctica (Fischer et al., 2007); MS records of (b) GC03-C1 (Bak et al., 2010), (c) MD07-3134 and MD07-3133 (Weber et al., 2012), (d) PS67/219-1 and PS67/197-1 (Xiao et al., 2016) from the Scotia Sea; and (e) MS (dark blue) and median destructive field of IRM ($MDF_{IRM}$; light blue) from PASADO Site 2 from Laguna Potrok Aike in Patagonia (Lisé-Pronovost et al., 2015). (For interpretation of the references to colour in this figure legend, the reader is referred to the web version of this article.)

continents to the Scotia Sea. Thus, current transport would not be the main transport mechanism for increasing coarse particles ranging from sand to coarse silt in the Scotia Sea, although it could result in a quantitative increase in fine-grained detritus input during the glacial period.

Mass flow such as turbidites can entrain coarse sand; however, turbidite deposition was not observed in the glacial intervals in GC03-C1 and nearby cores (Fig. 1; Kim et al., 2018b). Furthermore, the possibility of significant sediment redistribution (e.g., winnowing effect) by the bottom current was ruled out for south Scotia Sea sediments during the glacial period (Kim et al., 2018b). Sea ice extension or an advance of the ice-sheet grounding zone can deliver fine-grained detritus by trapping and resuspension, respectively; nevertheless, they would also fail to be the main transport mechanisms of coarser silts and sands (Weber et al., 2012; Kim et al., 2018b).

In this study, IRD is considered as the most plausible transport mechanism capable of delivering sand- to silt-sized sediments during the glacial period. Kim et al. (2018b) suggested iceberg calving activity as the main contributor to the high MS of glacial sediments in the south Scotia Sea, because the particle-size distribution of the dominant silt mode is very similar to that of IRD modeled from the subarctic icebergs (Jonkers et al., 2015). For GC03-C1, the dominance of silt-sized (16–63 μm) sediments carrying glacial MS can support the large input of silts by IRD influx. Of course, the IRD-related magnetic signals in silts can be diluted by other source of finer materials, such as current and/or dust. Thus, the sand fraction with enriched magnetic minerals (SIRM; Fig. 6f) can be considered to retain strong IRD-related magnetic signals, despite its low fractional abundance. In particular, the sand fraction retains relatively concentrated hematite than finer fractions (HIRM; Fig. 6f), which characterizes IRD-derived sediments containing hematite. Such hematite contribution could highlight IRD-related signals in bulk sediment, compared to magnetite influenced by various origins.

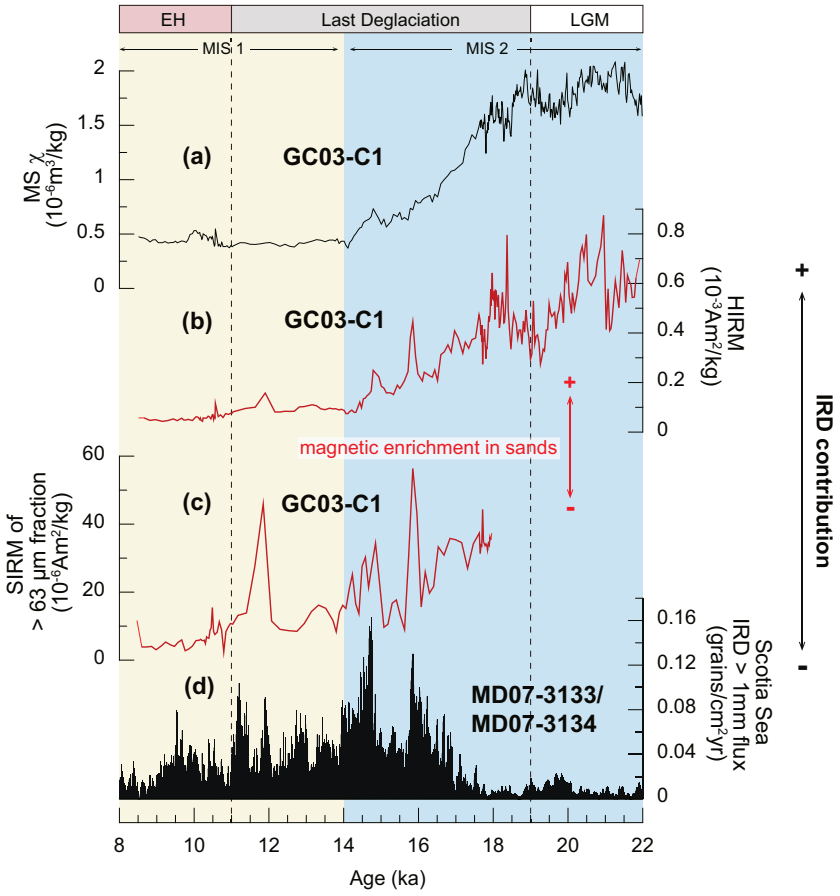


**Fig. 9.** Comparison between magnetic concentration parameters for core GC03-C1 and Scotia Sea iceberg rafted debris (IRD) flux from Weber et al. (2014). (a) χ and (b) HIRM for GC03-C1 bulk sediments; (c) SIRM of the > 63 μm fraction of GC03-C1; and (d) integrated flux of IRD coarser than 1 mm (IRD > 1 mm flux) for cores MD07-3133 and MD07-3134 (Weber et al., 2014).

Bulk HIRM of GC03-C1 is compared with the IRD flux previously reported for the Scotia Sea for the last ~22 kyr (Fig. 9); Weber et al. (2014) proposed a high-resolution IRD flux, based on counts of grains coarser than 1 mm from sediment cores in the central Scotia Sea (IRD > 1 mm flux; Fig. 9d). The IRD > 1 mm flux is strikingly high during the deglacial period (~17–9 ka), consistent with the timing of the iceberg retreat related to deglacial warming. This deglacial fluctuation of the IRD > 1 mm flux is very similar to that of bulk HIRM of GC03-C1 (Fig. 9b), which is more highlighted in the magnetic mineral enrichment in the sand fraction (SIRM of > 63 μm fraction; Fig. 9c). This strongly indicates a simultaneous IRD influx into widespread Scotia Sea sediments, while also supporting that IRD influx results in the enrichment of magnetic minerals, both magnetite and hematite. Such abundant magnetic minerals of IRD could be related to potential source rock property in Antarctica (e.g., Pirrung et al., 2002; Brachfeld et al., 2013). In previous petrographic/mineralogical studies, origin of IRD clasts in Scotia Sea sediments was inferred as magmatic and metasedimentary rocks in the Antarctic Peninsula (Conolly and Ewing, 1965; Diekmann et al., 2000). However, a simulated model of Antarctic ice-loss reveals that the IRD (> 1 mm) input time series in the Scotia Sea can be influenced from various sectors of ice-sheet discharge (e.g., the Weddell and Ross Seas), as icebergs merge together through the Iceberg Alley (Weber et al., 2014; Golledge et al., 2014).

Weber et al. (2014) suggested weak iceberg discharge during the last glacial period, as the flux of grains > 1 mm is very low (Fig. 9d). Although IRD input generally has been estimated by the number of grains coarser than 1 mm or 2 mm in the Scotia Sea (e.g., Diekmann et al., 2000; Weber et al., 2014), such method biased toward coarser gravel cannot fully evaluate the entire IRD contribution with various particle sizes. Alternatively, magnetic concentration, such as the bulk hematite contribution, could reflect relative contribution of the IRD-derived grains distributed in all sizes. Indeed, common peaks of SIRM, HIRM, and $\chi_{ARM}$ found in the bulk sediments during the last deglaciation is associated with magnetic peaks in the sand and silt fraction (Figs. 3 and 6d–k), indicating an IRD-related peak. Therefore, the glacial increase in magnetic concentration reflects that highly introduced fine IRD grains (fine sand to coarse silt) into sediments. The inconsistency between the low input of coarse (> 1 mm) grains and high input of finer IRD grains during the glacial period requires a more comprehensive understanding of the IRD input mechanism related to climate change. For instance, Kim et al. (2018b) suggested a different IRD input mechanism between the time of ice-sheet advance and retreat, which could supply vigorous finer IRD input at the margin of the ice shelf during glacial ice-sheet advances. To confirm such an unknown mechanism, various sedimentological and mineralogical studies would be needed; IRD provenance discrimination using geochemical indices will also be useful. Nevertheless, our results based on bulk and particle-size dependent magnetic properties clearly show that the higher concentration of magnetic minerals (e.g., high MS and HIRM values) during the glacial period is mainly caused by IRD input, implying active glacial iceberg discharge in the Scotia Sea. In addition, this further suggests cryosphere–atmosphere interactions, as shown by synchronization between MS and dust records.

## 7. Conclusion

Magnetic properties of bulk sediments and three particle-size fractions (> 63, 16–63, and < 16 μm) of Scotia Sea sediments were investigated over the past 22 kyr. In bulk sediments, concentration-related magnetic parameters (χ, $M_s$, SIRM, HIRM, and $\chi_{ARM}$) show similar variations with distinct glacial highs and interglacial lows, indicating a glacial increase in both the magnetite and hematite concentrations. Both magnetic mineral assemblages and grain size analyses indicate the dominance of coarse vortex/MD detrital magnetite in bulk and coarse

silt (16–63 μm) sediments during the glacial period. The glacial increase in bulk magnetic concentration is mainly contributed by the silt fraction, but it is also associated with the significant enrichment of magnetic minerals in the sand (> 63 μm) fraction. Moreover, magnetic concentration between silts and sands covaries throughout the last deglaciation, indicating the same sediment transport mechanisms. As the most plausible mechanism capable of transporting sediment particles ranging from sand to coarse silt, IRD input is considered. As hematite is relatively concentrated in the sand fraction (i.e., high HIRM values) during the glacial period, HIRM of bulk sediment can highlight IRD-related signal. The bulk HIRM variation could reflect the IRD contribution in various sediment particle-size, and thus its glacial increase suggests a considerable IRD input by active iceberg calving, resulting in high magnetic concentration.

Supplementary data to this article can be found online at https://doi.org/10.1016/j.palaeo.2020.109906.

## Declaration of Competing Interest

The authors declare that they have no known competing financial interests or personal relationships that could have appeared to influence the work reported in this paper.

## Acknowledgements

We would like to thank the crew and scientific party of the R/V *Yuzhmorgeologiya* for all their help during the gravity coring on board. FORC and IRM measurements were made in KIGAM, South Korea, through instrumental support from the Geological Research Division. We appreciate the handling editor (Dr. Paul Hesse) and two anonymous reviewers for their important and constructive comments to improve the manuscript. This research was supported by KOPRI project (PE20180).

## References

Anderson, J.B., Andrews, J.T., 1999. Radiocarbon constraints on ice sheet advance and retreat in the Weddell Sea, Antarctica. Geology, 27 (2), 179–182. https://doi.org/10.1130/0091-7613(1999)027<0179:RCOISA>2.3.CO;2.

Anderson, R.F., Ali, S., Bradtmiller, L.I., Nielsen, S.H.H., Fleisher, M.Q., Anderson, B.E., Burckle, L.H., 2009. Wind-driven upwelling in the Southern Ocean and the deglacial rise in atmospheric CO2. Science 323, 1443–1448. https://doi.org/10.1126/science.1167441.

Bak, Y., Lee, J., Yoon, H.I., Yoo, K., Lee, S., 2010. Holocene paleoclimate change in the area around Elephant Island, Antarctica: Evidence from the diatom record. J. Geol. Soc. Korea 46, 111–117.

Bareille, G., Grousset, F.E., Labracherie, M., Labeyrie, L.D., Petit, J.-R., 1994. Origin of detrital fluxes in the southeast Indian Ocean during the last climatic cycles. Paleoceanography 9, 799–819. https://doi.org/10.1029/94PA01946.

Bloemendal, J., King, J.W., Hall, F.R., Doh, S.-J., 1992. Rock magnetism of Late Neogene and Pleistocene deep-sea sediments: relationship to sediment source, diagenetic processes, and sediment lithology. J. Geophys. Res. 97, 4361–4375. https://doi.org/10.1029/91JB03068.

Brachfeld, S., Pinzon, J., Darley, J., Sagnotti, L., Kuhn, G., Florindo, F., Wilson, G., Ohneiser, C., Monien, D., Joseph, L., 2013. Iron oxide tracers of ice sheet extent and sediment provenance in the ANDRILL AND-1B drill core, Ross Sea, Antarctica. Glob. Planet. Change 110, 420–433. https://doi.org/10.1016/j.gloplacha.2013.09.015.

Carter-Stiglitz, B., Moskowitz, B., Jackson, M., 2001. Unmixing magnetic assemblages and the magnetic behavior of bimodal mixtures. J. Geophys. Res. Solid Earth 106, 26397–26411. https://doi.org/10.1029/2001JB000417.

Chang, L., Roberts, A.P., Heslop, D., Hayashida, A., Li, J., Zhao, X., Tian, W., Huang, Q., 2016. Widespread occurrence of silicate-hosted magnetic mineral inclusions in marine sediments and their contribution to paleomagnetic recording. J. Geophys. Res. Solid Earth 121, 8415–8431. https://doi.org/10.1002/2016JB013109.

Conolly, J.R., Ewing, M., 1965. Ice-rafted detritus as a climatic indicator in Antarctic deep-sea cores. Science 150 (80), 1822–1824. https://doi.org/10.1126/science.150.3705.1822.

Day, R., Fuller, M., Schmidt, V.A., 1977. Hysteresis properties of titanomagnetites: Grain-size and compositional dependence. Phys. Earth Planet. Inter. 13, 260–267. https://doi.org/10.1016/0031-9201(77)90108-X.

Dearing, J.A., Dann, R.J.L., Hay, K., Lees, J.A., Loveland, P.J., Maher, B.A., O'Grady, K., 1996. Frequency-dependent susceptibility measurements of environmental materials. Geophys. J. Int. 124, 228–240. https://doi.org/10.1111/j.1365-246X.1996.tb06366.x.

Delmonte, B., Andersson, P.S., Hansson, M., Schöberg, H., Petit, J.R., Basile-Doelsch, I., Maggi, V., 2008. Aeolian dust in East Antarctica (EPICA-Dome C and Vostok): Provenance during glacial ages over the last 800 kyr. Geophys. Res. Lett. 35, 256–264. https://doi.org/10.1029/2008GL033382.

Diekmann, B., Kuhn, G., Rachold, V., Abelmann, A., Brathauer, U., Fütterer, D.K., Gersonde, R., Grobe, H., 2000. Terrigenous sediment supply in the Scotia Sea (Southern Ocean): response to Late Quaternary ice dynamics in Patagonia and on the Antarctic Peninsula. Palaeogeogr. Palaeoclimatol. Palaeoecol. 162, 357–387. https://doi.org/10.1016/S0031-0182(00)00138-3.

Diekmann, B., Fütterer, D.K., Grobe, H., Hillenbrand, C.D., Kuhn, G., Michels, K., Petschick, R., Pirrung, M., 2003. Terrigenous sediment supply in the polar to Temperate South Atlantic: Land-ocean links of environmental changes during the Late Quaternary. In: The South Atlantic in the Late Quaternary. Springer Berlin Heidelberg, Berlin, Heidelberg, pp. 375–399. https://doi.org/10.1007/978-3-642-18917-3_18.

Domack, E.W., Jacobson, E.A., Shipp, S., Anderson, J.B., 1999. Late Pleistocene-Holocene retreat of the West Antarctic Ice-Sheet system in the Ross Sea: Part 2 - Sedimentologic and stratigraphic signature. Bull. Geol. Soc. Am. 111, 1517–1536. https://doi.org/10.1130/0016-7606(1999)111<1517:LPHROT>2.3.CO;2.

Dunlop, D.J., 1986. Coercive forces and coercivity spectra of submicron magnetites. Earth Planet. Sci. Lett. 78, 288–295. https://doi.org/10.1016/0012-821X(86)90068-3.

Dunlop, D.J., 2002. Theory and application of the Day plot (Mrs/Ms versus Hcr/Hc) 1. Theoretical curves and tests using titanomagnetite data. J. Geophys. Res. 107. https://doi.org/10.1029/2001JB000486.

Dunlop, D.J., Carter-Stiglitz, B., 2006. Day plots of mixtures of superparamagnetic, single-domain, pseudosingle-domain, and multidomain magnetites. J. Geophys. Res. Solid Earth 111, B12S09. https://doi.org/10.1029/2006JB004499.

Egli, R., 2003. Analysis of the field dependence of remanent magnetization curves. J. Geophys. Res. Solid Earth 108, 1–25. https://doi.org/10.1029/2002JB002023.

Egli, R., 2013. VARIFORC: An optimized protocol for calculating non-regular first-order reversal curve (FORC) diagrams. Glob. Planet. Change 110, 302–320. https://doi.org/10.1016/j.gloplacha.2013.08.003.

Egli, R., Chen, A.P., Winklhofer, M., Kodama, K.P., Horng, C.-S., 2010. Detection of noninteracting single domain particles using first-order reversal curve diagrams. Geochem. Geophys. Geosyst. 11, Q01Z11. https://doi.org/10.1029/2009GC002916.

Feinberg, J.M., Scott, G.R., Renne, P.R., Wenk, H.-R., 2005. Exsolved magnetite inclusions in silicates: Features determining their remanence behavior. Geology 33, 513–516. https://doi.org/10.1130/G21290.1.

Fischer, H., Fundel, F., Ruth, U., Twarloh, B., Wegner, A., Udisti, R., Becagli, S., Castellano, E., Morganti, A., Severi, M., Wolff, E., Littot, G., Röthlisberger, R., Mulvaney, R., Hutterli, M.A., Kaufmann, P., Federer, U., Lambert, F., Bigler, M., Hansson, M., Jonsell, U., de Angelis, M., Boutron, C., Siggaard-Andersen, M.-L., Steffensen, J.P., Barbante, C., Gaspari, V., Gabrielli, P., Wagenbach, D., 2007. Reconstruction of millennial changes in dust emission, transport and regional sea ice coverage using the deep EPICA ice cores from the Atlantic and Indian Ocean sector of Antarctica. Earth Planet. Sci. Lett. 260, 340–354. https://doi.org/10.1016/j.epsl.2007.06.014.

Gersonde, R., Crosta, X., Abelmann, A., Armand, L., 2005. Sea-surface temperature and sea ice distribution of the Southern Ocean at the EPILOG Last Glacial Maximum—a circum-Antarctic view based on siliceous microfossil records. Quat. Sci. Rev. 24, 869–896. https://doi.org/10.1016/j.quascirev.2004.07.015.

Golledge, N.R., Menviel, L., Carter, L., Fogwill, C.J., England, M.H., Cortese, G., Levy, R.H., 2014. Antarctic contribution to meltwater pulse 1A from reduced Southern Ocean overturning. Nat. Commun. 5, 5107. https://doi.org/10.1038/ncomms6107.

Harrison, R.J., Feinberg, J.M., 2008. FORCinel: An improved algorithm for calculating first-order reversal curve distributions using locally weighted regression smoothing. Geochem. Geophys. Geosyst. 9, Q05016. https://doi.org/10.1029/2008GC001987.

Hatfield, R.G., Reyes, A.V., Stoner, J.S., Carlson, A.E., Beard, B.L., Winsor, K., Welke, B., 2016. Interglacial responses of the southern Greenland ice sheet over the last 430,000 years determined using particle-size specific magnetic and isotopic tracers. Earth Planet. Sci. Lett. 454, 225–236. https://doi.org/10.1016/j.epsl.2016.09.014.

Hatfield, R.G., Stoner, J.S., Reilly, B.T., Tepley, F.J., Wheeler, B.H., Housen, B.A., 2017. Grain size dependent magnetic discrimination of Iceland and South Greenland terrestrial sediments in the northern North Atlantic sediment record. Earth Planet. Sci. Lett. 474, 474–489. https://doi.org/10.1016/j.epsl.2017.06.042.

Hatfield, R.G., Wheeler, B.H., Reilly, B.T., Stoner, J.S., Housen, B.A., 2019. Particle size specific magnetic properties across the Norwegian-Greenland Seas: Insights into the influence of sediment source and texture on bulk magnetic records. Geochem. Geophys. Geosyst. 20, 1004–1025. https://doi.org/10.1029/2018GC007894.

Hemming, S.R., van de Flierdt, T., Goldstein, S.L., Franzese, A.M., Roy, M., Gastineau, G., Landrot, G., 2007. Strontium isotope tracing of terrigenous sediment dispersal in the Antarctic circumpolar current: implications for constraining frontal positions. Geochem. Geophys. Geosyst. 8, Q06N13. https://doi.org/10.1029/2006GC001441.

Hounslow, M.W., Maher, B.A., 1996. Quantitative extraction and analysis of carriers of magnetization in sediments. Geophys. J. Int. 124, 57–74. https://doi.org/10.1111/j.1365-246X.1996.tb06352.x.

Hyland, E.G., Sheldon, N.D., Van der Voo, R., Badgley, C., Abrajevitch, A., 2015. A new paleoprecipitation proxy based on soil magnetic properties: implications for expanding paleoclimate reconstructions. Geol. Soc. Am. Bull. 127, B31207.1. https://doi.org/10.1130/B31207.1.

Jonkers, L., Barker, S., Hall, I.R., Prins, M.A., 2015. Correcting for the influence of ice-rafted detritus on grain size-based paleocurrent speed estimates. Paleoceanography 30, 1347–1357. https://doi.org/10.1002/2015PA002830.

Jouve, G., Lisé-Pronovost, A., Francus, P., De Coninck, A.S., 2017. Climatic influence of the latest Antarctic isotope maximum of the last glacial period (AIM4) on Southern Patagonia. Palaeogeogr. Palaeoclimatol. Palaeoecol. 472, 33–50. https://doi.org/10.

1016/j.palaeo.2017.02.020.
Kim, S., Yoo, K.-C., Lee, J.I., Khim, B.-K., Bak, Y.-S., Lee, M.K., Lee, J., Domack, E.W., Christ, A.J., Yoon, H.I., 2018a. Holocene paleoceanography of Bigo Bay, west Antarctic Peninsula: Connections between surface water productivity and nutrient utilization and its implication for surface-deep water mass exchange. Quat. Sci. Rev. 192, 59–70. https://doi.org/10.1016/j.quascirev.2018.05.028.
Kim, S., Yoo, K.-C., Lee, J.I., Lee, M.K., Kim, K., Yoon, H.I., Moon, H.S., 2018b. Relationship between magnetic susceptibility and sediment grain size since the last glacial period in the Southern Ocean off the northern Antarctic Peninsula – Linkages between the cryosphere and atmospheric circulation. Palaeogeogr. Palaeoclimatol. Palaeoecol. 505, 359–370. https://doi.org/10.1016/j.palaeo.2018.06.016.
King, J., Banerjee, S.K., Marvin, J., Özdemir, Ö., 1982. A comparison of different magnetic methods for determining the relative grain size of magnetite in natural materials: Some results from lake sediments. Earth Planet. Sci. Lett. 59, 404–419. https://doi.org/10.1016/0012-821X(82)90142-X.
Kohfeld, K.E., Graham, R.M., De Boer, A.M., Sime, L.C., Wolff, E.W., Le Quéré, C., Bopp, L., 2013. Southern Hemisphere westerly wind changes during the Last Glacial Maximum: Paleo-data synthesis. Quat. Sci. Rev. 68, 76–95.
Lambert, F., Bigler, M., Steffensen, J.P., Hutterli, M., Fischer, H., 2012. Centennial mineral dust variability in high-resolution ice core data from Dome C, Antarctica. Clim. Past 8, 609–623. https://doi.org/10.5194/cp-8-609-2012.
Lamy, F., Kilian, R., Arz, H.W., Francois, J.-P., Kaiser, J., Prange, M., Steinke, T., 2010. Holocene changes in the position and intensity of the southern westerly wind belt. Nat. Geosci. 3, 695–699. https://doi.org/10.1038/ngeo959.
Lamy, F., Gersonde, R., Winckler, G., Esper, O., Jaeschke, A., Kuhn, G., Ullermann, J., Martinez-Garcia, A., Lambert, F., Kilian, R., 2014. Increased dust deposition in the Pacific Southern Ocean during Glacial periods. Science 343 (80), 403–407. https://doi.org/10.1126/science.1245424.
Lamy, F., Arz, H.W., Kilian, R., Lange, C.B., Lembke-Jene, L., Wengler, M., Kaiser, J., Baeza-Urrea, O., Hall, I.R., Harada, N., Tiedemann, R., 2015. Glacial reduction and millennial-scale variations in Drake Passage throughflow. Proc. Natl. Acad. Sci. 112, 13496–13501. https://doi.org/10.1073/pnas.1509203112.
Lascu, I., Banerjee, S.K., Berquó, T.S., 2010. Quantifying the concentration of ferrimagnetic particles in sediments using rock magnetic methods. Geochem. Geophys. Geosyst. 11. https://doi.org/10.1029/2010GC003182.
Lee, J.I., Bak, Y.-S., Yoo, K.-C., Lim, H.S., Yoon, H.I., Yoon, H.S., 2010. Climate changes in the South Orkney Plateau during the last 8600 years. The Holocene 20, 395–404. https://doi.org/10.1177/0959683609353430.
Lisé-Pronovost, A., St-Onge, G., Gogorza, C., Haberzettl, T., Jouve, G., Francus, P., Ohlendorf, C., Gebhardt, C., Zolitschka, B., 2015. Rock-magnetic proxies of wind intensity and dust since 51,200 cal BP from lacustrine sediments of Laguna Potrok Aike, southeastern Patagonia. Earth Planet. Sci. Lett. 411, 72–86. https://doi.org/10.1016/j.epsl.2014.11.007.
Maher, B.A., 1986. Characterisation of soils by mineral magnetic measurements. Phys. Earth Planet. Inter. 42, 76–92. https://doi.org/10.1016/S0031-9201(86)80010-3.
Maher, B.A., 1988. Magnetic properties of some synthetic sub-micron magnetites. Geophys. J. Int. 94, 83–96. https://doi.org/10.1111/j.1365-246X.1988.tb03429.x.
Maher, B.A., Alekseev, A., Alekseeva, T., 2003. Magnetic mineralogy of soils across the Russian Steppe: climatic dependence of pedogenic magnetite formation. Palaeogeogr. Palaeoclimatol. Palaeoecol. 201, 321–341. https://doi.org/10.1016/S0031-0182(03)00618-7.
Maher, B.A., Prospero, J.M., Mackie, D., Gaiero, D., Hesse, P.P., Balkanski, Y., 2010. Global connections between aeolian dust, climate and ocean biogeochemistry at the present day and at the last glacial maximum. Earth-Sci. Rev. 99, 61–97. https://doi.org/10.1016/j.earscirev.2009.12.001.
Maxbauer, D.P., Feinberg, J.M., Fox, D.L., 2016. MAX UnMix: A web application for unmixing magnetic coercivity distributions. Comput. Geosci. 95, 140–145. https://doi.org/10.1016/j.cageo.2016.07.009.
McCave, I.N., Crowhurst, S.J., Kuhn, G., Hillenbrand, C.-D., Meredith, M.P., 2014. Minimal change in Antarctic Circumpolar Current flow speed between the last glacial and Holocene. Nat. Geosci. 7, 113–116. https://doi.org/10.1038/ngeo2037.
Muhs, D.R., 2013. The geologic records of dust in the Quaternary. Aeolian Res. 9, 3–48. https://doi.org/10.1016/j.aeolia.2012.08.001.
Mullins, C.E., 1977. Magnetic susceptibility of the soil and its significance in soil science - A review. J. Soil Sci. 28, 223–246. https://doi.org/10.1111/j.1365-2389.1977.tb02232.x.
Noble, T.L., Piotrowski, A.M., Robinson, L.F., McManus, J.F., Hillenbrand, C.-D., Bory, A.J.M., 2012. Greater supply of Patagonian-sourced detritus and transport by the ACC to the Atlantic sector of the Southern Ocean during the last glacial period. Earth Planet. Sci. Lett. 317–318, 374–385. https://doi.org/10.1016/j.epsl.2011.10.007.
Orsi, A.H., Whitworth, T., Nowlin, W.D., 1995. On the meridional extent and fronts of the Antarctic Circumpolar Current. Deep Sea Res. Part I Oceanogr. Res. Pap. 42, 641–673. https://doi.org/10.1016/0967-0637(95)00021-W.
Pirrung, M., Hillenbrand, C.D., Diekmann, B., Fütterer, D., Grobe, H., Kuhn, G., 2002. Magnetic susceptibility and ice-rafted debris in surface sediments of the Atlantic sector of the Southern Ocean. Geo-Marine Lett. 22, 170–180. https://doi.org/10.1007/s00367-002-0109-7.
Pugh, R.S., McCave, I.N., Hillenbrand, C.-D., Kuhn, G., 2009. Circum-Antarctic age modelling of Quaternary marine cores under the Antarctic Circumpolar Current: ice-core dust–magnetic correlation. Earth Planet. Sci. Lett. 284, 113–123. https://doi.org/10.1016/j.epsl.2009.04.016.
Razik, S., Dekkers, M.J., von Dobeneck, T., 2014. How environmental magnetism can enhance the interpretational value of grain-size analysis: A time-slice study on sediment export to the NW African margin in Heinrich Stadial 1 and Mid Holocene. Palaeogeogr. Palaeoclimatol. Palaeoecol. 406, 33–48. https://doi.org/10.1016/j.palaeo.2014.04.009.
Razik, S., Govin, A., Chiessi, C.M., von Dobeneck, T., 2015. Depositional provinces, dispersal, and origin of terrigenous sediments along the SE South American continental margin. Mar. Geol. 363, 261–272. https://doi.org/10.1016/j.margeo.2015.03.001.
Reimer, P.J., Bard, E., Bayliss, A., Beck, J.W., Blackwell, P.G., Ramsey, C.B., Buck, C.E., Cheng, H., Edwards, R.L., Friedrich, M., Grootes, P.M., Guilderson, T.P., Haflidason, H., Hajdas, I., Hatté, C., Heaton, T.J., Hoffmann, D.L., Hogg, A.G., Hughen, K.A., Kaiser, K.F., Kromer, B., Manning, S.W., Niu, M., Reimer, R.W., Richards, D.A., Scott, E.M., Southon, J.R., Staff, R.A, Turney, C.S.M., van der Plicht, J., 2013. IntCal13 and Marine13 radiocarbon age calibration curves 0–50,000 years cal BP. Radiocarbon 55, 1869–1887.
Roberts, A.P., Cui, Y., Verosub, K.L., 1995. Wasp-waisted hysteresis loops: Mineral magnetic characteristics and discrimination of components in mixed magnetic systems. J. Geophys. Res. Solid Earth 100, 17909–17924. https://doi.org/10.1029/95JB00672.
Roberts, A.P., Heslop, D., Zhao, X., Pike, C.R., 2014. Understanding fine magnetic particle systems through use of first-order reversal curve diagrams. Rev. Geophys. 52, 557–602. https://doi.org/10.1002/2014RG000462.
Roberts, A.P., Almeida, T.P., Church, N.S., Harrison, R.J., Heslop, D., Li, Y., Li, J., Muxworthy, A.R., Williams, W., Zhao, X., 2017. Resolving the origin of pseudo-single domain magnetic behavior. J. Geophys. Res. Solid Earth 122, 9534–9558. https://doi.org/10.1002/2017JB014860.
Strehlau, J.H., Hegner, L.A., Strauss, B.E., Feinberg, J.M., Penn, R.L., 2014. Simple and efficient separation of magnetic minerals from speleothems and other carbonates. J. Sediment. Res. 84, 1096–1106. https://doi.org/10.2110/jsr.2014.89.
Stuiver, M., Reimer, P.J., 1993. Extended 14C database and revised CALIB radiocarbon calibration program. Radiocarbon 35, 215–230.
Walter, H., Hegner, E., Diekmann, B., Kuhn, G., Rutgers van der loeff, M., 2000. Provenance and transport of terrigenous sediment in the south Atlantic Ocean and their relations to glacial and interglacial cycles: Nd and Sr isotopic evidence. Geochim. Cosmochim. Acta 64, 3813–3827. https://doi.org/10.1016/S0016-7037(00)00476-2.
Weber, M.E., Kuhn, G., Sprenk, D., Rolf, C., Ohlwein, C., Ricken, W., 2012. Dust transport from Patagonia to Antarctica – a new stratigraphic approach from the Scotia Sea and its implications for the last glacial cycle. Quat. Sci. Rev. 36, 177–188. https://doi.org/10.1016/j.quascirev.2012.01.016.
Weber, M.E., Clark, P.U., Kuhn, G., Timmermann, A., Sprenk, D., Gladstone, R., Zhang, X., Lohmann, G., Menviel, L., Chikamoto, M.O., Friedrich, T., Ohlwein, C., 2014. Millennial-scale variability in Antarctic ice-sheet discharge during the last deglaciation. Nature 510, 134–138. https://doi.org/10.1038/nature13397.
Weber, M.E., Raymo, M.E., Peck, V.L., Williams, T., 2019. Expedition 382 Preliminary Report: Iceberg Alley and Subantarctic Ice and Ocean Dynamics, International Ocean Discovery Program Preliminary Report. International Ocean Discovery Program. https://doi.org/10.14379/iodp.pr.382.2019.
Xiao, W., Frederichs, T., Gersonde, R., Kuhn, G., Esper, O., Zhang, X., 2016. Constraining the dating of late Quaternary marine sediment records from the Scotia Sea (Southern Ocean). Quat. Geochronol. 31, 97–118. https://doi.org/10.1016/j.quageo.2015.11.003.
Yamazaki, T., Ikehara, M., 2012. Origin of magnetic mineral concentration variation in the Southern Ocean. Paleoceanography 27, PA2206. https://doi.org/10.1029/2011PA002271.